ACS OMEGA

http://pubs.acs.org/journal/acsodf

Article

Reduced Graphene Oxide-Modified Spinel Cobalt Ferrite Nanocomposite: Synthesis, Characterization, and Its Superior Adsorption Performance for Dyes and Heavy Metals

Zafar Iqbal,* Mohd Saquib Tanweer, and Masood Alam*

Cite This: *ACS Omega* 2023, 8, 6376−6390

Read Online

ACCESS | Metrics & More | Article Recommendations | Supporting Information

ABSTRACT: This work is dedicated to the synthesis, characterization, and adsorption performance of reduced graphene oxide-modified spinel cobalt ferrite nanoparticles. The as-synthesized reduced graphene oxide cobalt ferrite (RGCF) nanocomposite has been characterized using FTIR spectroscopy, FESEM coupled with EDXS, XRD, HRTEM, zeta potential, and vibrating sample magnetometer (VSM) measurements. FESEM proves the particle size in the range of 10 nm. FESEM, EDX, TEM, FTIR, and XPS analyses provide the proof of successful incorporation of rGO sheets with cobalt ferrite nanoparticles. The crystallinity and spinel phase of cobalt ferrite nanoparticles have been shown by XRD results. The saturation magnetization (M_s) was measured as 23.62 emu/g, proving the superparamagnetic behavior of RGCF. The adsorption abilities of the synthesized nanocomposite have been tested using cationic crystal violet (CV) and brilliant green (BG) and anionic methyl orange (MO) and Congo red (CR) dyes. The adsorption trend for MO, CR, BG, and As(V) follows RGCF > rGO > CF at neutral pH. Adsorption studies have been accomplished by optimizing parameters like pH (2−8), adsorbent dose (1−3 mg/25 mL), initial concentration (10−200 mg/L), and contact time at constant room temperature (RT). To further investigate the sorption behavior, isotherm, kinetics, and thermodynamic studies have been conducted. Langmuir isotherm and pseudo-second-order kinetic models suited better for the adsorption of dyes and heavy metals. The maximum adsorption capacities (q_m) obtained have been found as 1666.7, 1000, 416.6, and 222.2 mg/g for MO, CR, BG, and As, respectively, with operational parameters such as T = 298.15 K; RGCF dose: 1 mg for MO and 1.5 mg each for CR, BG, and As. Thus, the RGCF nanocomposite was found to be an excellent adsorbent for the removal of dyes and heavy metals.

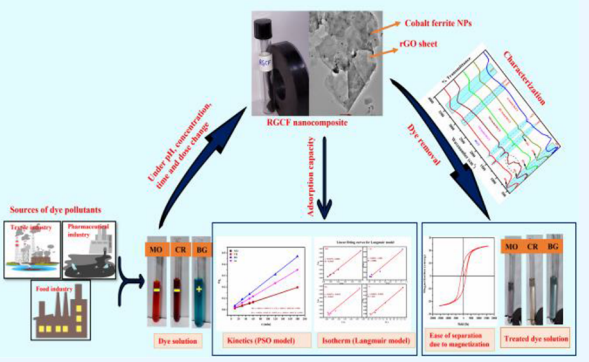

1. INTRODUCTION

The introduction of dyes, heavy metals, pharmaceutical drugs, and other pollutants into water bodies has been a global concern. There is a coexistence of heavy metals and dyes found often in wastewater streams that forms an important and toxic combination.[1,2] The surfaces of fabrics, papers, cosmetics, leather, and so forth are attached to the chemical compounds that impart color to them known as dyes. Dyes play an important role in human life. A number of industries, namely pharmaceutical, food, textile, leather, cosmetics, and paper release a large number of synthetic dyes.[3,4] Approximately 100 tonnes of dyes per year is discarded to water bodies in the form of waste. The annual production of commercial dyes from different industries is estimated to be about 7×10^5 tonnes. The severity of toxicity of such a large amount of disposal of dyes in aqueous media may cause a lethal effect to all living beings.[5] Dyes belong to a diverse synthetic origin and, therefore, their removal is quite challenging. The prolonged manifestation of these toxic dyes may lead to other implications, namely respiratory disorders, skin irritation, and even cancer. Furthermore, they are released into the environment causing pollution of aqueous media, leaving colored wastewater. Therefore, such effluents could also alter the process of photosynthesis and reduce light penetration, which directly or indirectly result in diminishing oxygen levels for aquatic creatures. As they impart toxicity to the water bodies, their content needs to be minimized before their discharge into water bodies to the permissible levels.[6,7] MO and CR are anionic benzidine-based azo dyes. They may cause allergy and get metabolized into a carcinogenic product "benzidine".[8] Both BG and CV are cationic triphenylmethane-type dyes. However, BG is used for several purposes, including antiseptics and biological stains. Its effluents are produced

Received: October 14, 2022
Accepted: February 3, 2023
Published: February 13, 2023

from textile dying, paper printing, rubber, and plastic industries. This dye is found to be quite hazardous in the cases of eyes, skin contact, and of course ingestion. It may emit carbon dioxide and oxides of sulfur and nitrogen during its decomposition.[9] However, CV is found to be highly toxic and mutagenic, which make it biohazardous. Even the presence of a small amount of 1 mg/L makes photosynthesis impossible due to its intense color.[10] Heavy metals are another class of pollutants that impart toxicity in wastewater. Among these pollutants, arsenic compounds are widely known for their toxicity in the environment matrix. The presence of arsenic could be in more toxic inorganic forms such as As(V) (arsenate) and As(III) (arsenite).[11] Environmental submission of arsenic imposes a severe health issue worldwide. Groundwater contamination with arsenic is considered the main source of exposure to both humans and animals. A concentration of as low as 10 ppm of inorganic arsenic exposure can cause skin, lung, and bladder cancers. Hyperkeratosis, atherosclerosis, diabetes, and chronic obstructive pulmonary diseases are some noncancerous diseases which may be caused due to mild arsenic exposure.[12] Finding an efficient and cost-effective method to remove cationic and anionic dyes simultaneously is a challenging task. Different kinds of wastewater purification methods have been employed, namely, adsorption.[13,14] biological degradation,[15] and chemical oxidation.[16] Adsorptive removal is a relatively inexpensive, highly efficient, and fast approach for wastewater treatment. It is also less sensitive to toxic substances and easy to perform.[14] In recent years, a wide array of materials has been used as adsorbents, including agricultural residues, mesoporous silica, kaolin, gelatin fiber, and activated carbon. Despite their similarities, these materials still struggle with aqueous solution separation. In spite of the fact that adsorption uses much of the carbonaceous material alone and is recyclable, it may block filters if used too often. In order to address the above-mentioned difficulties in separation and preparation, ferrite, based specifically on cobalt ferrite, which is easy to prepare and has moderate magnetic properties, could be considered as a potential solution.[17] Modified metal oxide (polymeric, surfactant-assisted, and carbonaceous) nanocomposites have a relatively better capability of removing pollutants from wastewater.[13,18] To check secondary pollution, a carbonaceous material is incorporated with magnetic materials, leading the nanocomposite to the next level due to the introduction of the magnetic nature. Magnetic graphene oxide nanocomposite is considered one among them.[19,20] The modified form of graphite, such as graphene, is a class of two-dimensional carbon nanostructures which may consist of one or many layers of atomic graphite. It bears tremendous electrical, thermal, and mechanical properties. Besides these, it has an excellent surface area of 2630 m^2/g and graphitized basal plane.[21] Its wide application area includes but not limited to the fabrication of optoelectronic devices,[22] supercapacitors,[23] hydrogen storage, batteries,[24] sensors,[25] solar cells,[26] and wastewater treatment.[27] Despite all attributes, there are some negative consequences, which include separation inconvenience. Nanoadsorbents with a magnetic nature are a class of adsorbents which already have an advantage of being magnetically separable. GO comprises an aggregating nature; therefore, its incorporation with metal oxides provides a proficient way to make ecofriendly composites. Graphene in turn has an ultra-large surface area to be a perfect adsorbent. Therefore, to make facile separation, GO/rGO is introduced with the magnetic species of metal oxides.[28] Among the spinel form of ferrites, cobalt ferrite ($CoFe_2O_4$) is a highly known form studied due to its mechanical hardness, moderate saturation magnetization, high coercivity, and chemical stability.[29] Cobalt ferrite ($CoFe_2O_4$) bears a spinel crystallographic structure which exhibits superior magnetic behavior.[20] Literature review from the past reveals that most of the efforts have been made to remove either anionic or cationic dyes at some pH. For instance, Yavari et al. reported the adsorption of anionic dyes direct red 80 (DR 80), direct green 6 (DG 6), and acid blue 92 (AB 92) by cobalt ferrite nanoparticles (CFNPs) and their modified forms. All the three anionic dyes are textile dyes. The results of this study show that the modified forms could effectively remove the dyes.[30] El-Shafai et al. demonstrated the adsorptive removal of the cationic dye "Rhodamine B (RhB)" by GO metal oxide nanocomposites ($GO-Fe_3O_4@ZrO_2$). The anionic surface of the GO nanocomposite exhibits ~ 93% efficiency of adsorption.[31] Guo et al. presented a study over a sandwiched nanostructure of Fe_3O_4/carboxylate graphene oxide. They demonstrated better adsorption capacity for methylene blue and Rhodamine B (RhB) dyes of 35.958 and 22.124 mg/g, respectively, due to the sandwiched structure and better specific surface area.[32] However, there are also few reports on the removal of both cationic and anionic dyes. Ibrahim et al. investigated the adsorptive elimination of anionic remazole red (RR-133) and cationic methylene blue (MB). Their result data show that cobalt iron oxide modified by humic acid ($CoFe_2O_4$-HA) has greater adsorption rate.[33] Du et al. presented a study on the superior adsorption performance of anionic and cationic dyes by the PVP-modified $rGO/CoFe_2O_4$ nanocomposite.[34]

In this paper, Figure S4 shows the adsorption behavior of rGO, cobalt ferrite, and $rGO/CoFe_2O_4$ (RGCF) nanocomposites. The adsorption efficiency trend was found to be RGCF > rGO > $CoFe_2O_4$ NPs. Figure S2 shows the digital images before and after the adsorption of dyes with optimized results. We took the benefit of the high surface area of GO and the magnetic properties of spinel cobalt ferrite nanoparticles to improve the adsorption efficiencies of the wastewater contaminants and ease of separation. The kinetic, isotherm, and thermodynamic studies were performed for the better understanding of the interaction of RGCF nanocomposites and the adsorbate molecules (dyes and heavy metal). The as-prepared RGCF nanocomposite hence displays the excellent separation and adsorption capacity of toxic dyes (cationic and anionic) and heavy metals from aqueous solution.

2. MATERIALS AND METHODS

2.1. Materials. MO, CR, BG, CV, and graphite powder were purchased from Loba Chemie India. Cobalt chloride hexahydrate [$CoCl_2.6H_2O$] and iron chloride hexahydrate [$FeCl_3.6H_2O$] were purchased from Sigma Aldrich. Standard samples were prepared in the laboratory. Sulfuric acid (H_2SO_4, 98%), hydrogen peroxide (H_2O_2, 30%), potassium permanganate ($KMnO_4$), and sodium nitrate ($NaNO_3$) were purchased from Qualigens (Thermo Fischer Scientific India Pvt. Ltd.). All reagents used were of analytical (AR) grade. Double-distilled water (DDW) was used throughout the experiments. All chemicals were used without further purification. The characteristics of the model dyes used in this experiment are listed in Table 1.

2.2. Synthesis of rGO. Modified Hummers' route has been adopted for the synthesis of GO. To maintain the neutral pH,

https://doi.org/10.1021/acsomega.2c06636
ACS Omega 2023, 8, 6376−6390

Table 1. Characteristics of Model Dyes

dyes and their abbreviations	molar mass (g/mol)	molecular formula	λ_{max} (nm)
crystal violet (CV)	407.979	$C_{25}N_3H_{30}Cl$	590
Congo red (CR)	696.7	$C_{32}H_{22}N_6Na_2O_6S_2$	498
brilliant green (BG)	475.6	$C_{27}H_{34}N_2O_4S$	625
methyl orange (MO)	327.33	$C_{14}H_{14}N_3NaO_3S$	470

DDW was used.[35] The whole synthesis process has been accomplished in four different steps. First, 1 g of graphite powder is mixed with 0.5 g of $NaNO_3$. The mixture is then added into 100 mL of 98% cold H_2SO_4 in an ice bath to minimize the exothermic reaction. This is followed by a slow addition of 3 g $KMnO_4$ with constant stirring below 20 °C. The reaction was continued to proceed at 35 °C for 10 h; thereafter, 46 mL of ultrapure water was slowly added. This reaction was further continued for 15 more min at 98 °C. The mixture was then diluted to 140 mL with the addition of 2.5 mL of H_2O_2 (30 wt %) to remove the oxides of manganese. Finally, the cooled reaction mixture was filtered and washed three times with ultrapure water and alcohol and dried up at 70 °C for 12 h in a vacuum oven.

2.3. Synthesis of RGCF. The preparation of rGO/$CoFe_2O_4$ was performed by the coprecipitation of cobalt ferrite nanoparticles onto the surface of rGO particles. For this process, 0.126 g dry rGO was dispersed in 100 mL of pure water, followed by ultrasonication to get a stable suspension. Then, 0.72 g of cobalt nitrate hexahydrate and 2 g of iron nitrate nonahydrate were dissolved individually in 10 mL of water and combined to form a mixed iron salt solution. A 0.25 g of alcoholic CTAB solution was also added to the metal solution. Subsequently, ammonia solution (25 wt %) was added drop by drop to get a metal precipitate. pH of 10−11 is maintained during the precipitation. The metal precipitation was followed by the gradual addition of rGO suspension under stirring condition. The reaction is continued for 2 h at 80 °C. The solution was filtered and washed by DDW until neutral pH and dried at 100 °C for 10 h. The dried material was then calcined at 550 °C.

2.4. Characterization. The morphology of the prepared nanocomposite RGCF (before and after) was examined using a FESEM Zeiss (Gemini) instrument. Images of higher resolution were obtained from a transmission electron microscope (TECNAI G20, HR-TEM) operated at 200 kV. Elemental composition and elemental mapping were studied by an EDXS system coupled with a SEM instrument. The structural information and crystallinity were studied using an X-ray diffractometer (Rigaku TTRAX-III) with Cu K_α (λ = 1.5406 Å) at a scanning speed of 0.025°/s over the 2θ range of 10−80°. To study the functional group composition using KBr pellets in the range of 4000−400 cm^{-1}, FTIR analyses were done using Perkin Elmer Spectrum Two. Saturation magnetization and magnetic behavior were studied using a vibrating sample magnetometer (VSM)-7400 series instrument, Make: Lakeshore, USA, at room temperature. The zeta potential of the adsorbent was determined using Malvern Zetasizer Nano ZS to find out the charge on the nanomaterial.

3. RESULTS AND DISCUSSION

3.1. Characterization of RGCF. *3.1.1. X-ray Diffraction.* The XRD patterns in Figure 1a,b compare bare spinel cobalt ferrite and the composite of rGO-loaded spinel cobalt ferrite,

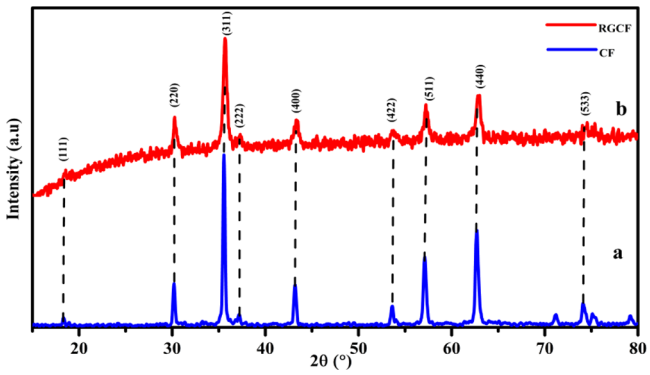

Figure 1. XRD patterns of (a) CF and (b) RGCF nanocomposites.

which show almost the same diffraction peaks and crystallinity. The absence of rGO peaks corresponds to their ultra-low quantity. These diffraction peaks show single-phase crystallinity. In both spinel cobalt ferrite and RGCF, the characteristic peaks at 2θ = 18.41°, 31.2°, 35.7°, 45.6°, 53.9°, 57.7°, 62.2°, and 74.3° confirm the cubic spinel planes of the respective crystals (111), (220), (311), (400), (422), (511), (440), and (533).

The crystal planes well matched with JCPDS card no (JCPDS 22-1086), confirming a FCC (face-centered cubic) spinel phase.[29,36] The average crystallite size was found to be 17.1 nm using Debye−Scherrer's formula with the FWHM value (full width half-maximum) at 2θ = 35.74 of the crystal plane (311). The value obtained from the XRD data well resonates with the mean particle size obtained from the TEM images.

Debye−Scherrer's equation[37]

$$p = \frac{0.9\lambda}{\beta\cos\theta} \quad (1)$$

where p = mean particle size, β = FWHM, and θ = Bragg angle.

3.1.2. FTIR Analysis. FTIR study (Figure 2) has been observed between 4000 and 400 cm^{-1}. Two stretching frequencies observed between 400 and 600 cm^{-1} correspond to the stretching vibrations of tetrahedral and octahedral metal oxygen bonding. The strong peak at a higher value of frequency of 574 cm^{-1} could be assigned to the stretching vibrations of the metal at the tetrahedral sites (Fe−O−Co),

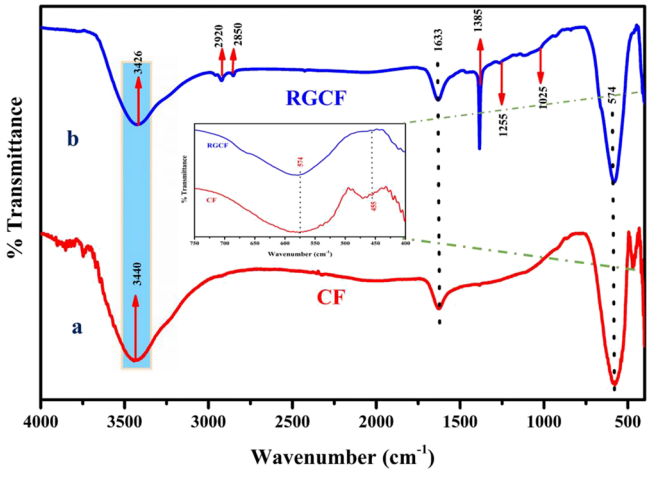

Figure 2. FTIR spectra of (a) CF and (b) RGCF nanocomposites.

https://doi.org/10.1021/acsomega.2c06636
ACS Omega 2023, 8, 6376−6390

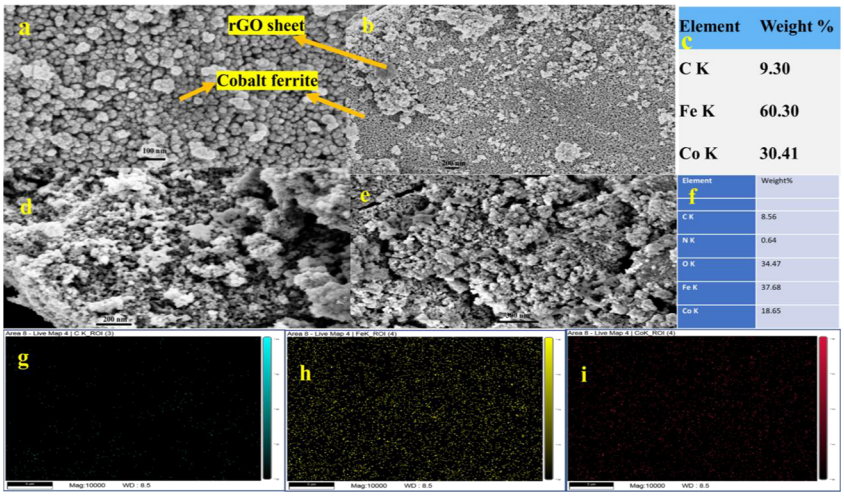

Figure 3. FESEM image of the RGCF nanocomposite (a, b) before adsorption and (d, e) after adsorption (dye loaded); (c) EDX before adsorption, (f) EDX after adsorption (dye loaded), and (g–i) elemental mapping of the RGCF nanocomposite.

while the stretching vibrations of the metal complex (Fe–O–Fe) appeared at a lower value of peak frequency of 455 cm^{-1} at the octahedral sites. The presence of these two peaks confirms the inverse spinel phase of $CoFe_2O_4$.[38,39] The broader peak observed at 3440 cm^{-1} in CF (Figure 2a) and 3426 cm^{-1} in RGCF (Figure 2b) can be indexed to the stretching vibrations, while the peak at 1633 cm^{-1} could be assigned to the bending vibrations of the hydroxyl groups of the water molecules. The peak at 1385 cm^{-1} could be assigned to the C–OH vibrational mode of rGO.[40] The peaks at 2925 and 2855 cm^{-1} could be ascribed to the asymmetric and symmetric CH_2 stretching vibrations, respectively, of rGO. The bands at 1255 and 1025 cm^{-1} denote the C–OH stretch of the alcohol group and C–O stretching vibrations from C–O–C, respectively, which can be related to rGO in the nanocomposite.[36] The lesser intensity peaks in between 1600 and 1700 cm^{-1} could be attributed to the COOH, C–OH, and C═O groups on rGO.[40] The presence of these characteristic peaks of rGO in the nanocomposite confirms the successful formation of RGCF.

In the case of CR adsorption, the FTIR spectrum of CR-loaded RGCF in the inset (Figure S1b) shows peaks at 1050 and 1162 cm^{-1} which could be assigned to the symmetric and asymmetric stretching vibrations of the sulfonate group (SO_3^-). The value of frequency is slightly lower as compared to the reported value for the unadsorbed dye due to the interaction of the dye with the adsorbent.[41,42] The peak at 1545 cm^{-1} frequency might be assigned to the stretching vibrations of the –N═N– group of diazo dyes (CR),[43] while the peak at 1426 cm^{-1} might be assigned to the aromatic skeletal vibrations.[44] The FTIR spectra of MO dye-loaded RGCF have been outlined in Figure S1c. The frequency obtained at 1114 cm^{-1} confirms the sulfonic nature of MO dye, while the peaks at 1384 and 1186 cm^{-1} could be assigned to –C–N stretching which corresponds to the azo nature of the dye. The peak at 1031 cm^{-1} corresponds to the –C–H stretching vibrations of the benzene ring.[45] In the FTIR spectra of BG-loaded RGCF (Figure S1d), the peaks at 1260, 1155, and 1060 cm^{-1} could be indexed to the aromatic ether (aryl-O) stretch, R–SO_3 (sulfonate), and C–O–C cyclic ether, respectively.[46] In both MO and CR dye adsorption, the presence of the characteristic sulfonate peaks at 1050, 1162 cm^{-1} (CR), and 1114 cm^{-1} (MO) suggests the successful adsorption of dyes onto the surface of RGCF. However, in the case of cationic species (BG and As ion), adsorption has been shown by either the shortening, shifting, or disappearance of peaks. Similar to the BG dye adsorption, the peak of C–OH present at 1385 cm^{-1} (Figure S1d) is shifted to 1384 cm^{-1} when compared to the adsorbent peak (Figure S1a).

However, the intensity of the –OH group of water molecules present at 1633 cm^{-1} and that of C–OH of rGO at 1384 cm^{-1} was found to be shortened. The shortening and shifting of these peaks show the adsorption of BG dye on RGCF. In the case of As (Figure S1e), the stretching vibration peak at around 583 cm^{-1} of metal oxide at the tetrahedral sites shows broadening, along with the shortening of hydroxyl functionalities of graphene moieties present at the frequencies of 1633 and 1385 cm^{-1}. This shows an electrostatic attraction as well as surface complexation with graphene sheets.

3.1.3. Morphological and Structural Analyses. 3.1.3.1. FESEM Analysis. The morphological and structural surveys of RGCF before and after adsorption have been elucidated by the FESEM study in Figure 3a–c. Cobalt ferrite nanoparticles attained a spherical shape with slight agglomeration, as can be seen in Figure 3a,b. Little agglomerations in cobalt ferrite nanoparticles of RGCF could be possibly due to the magnetic forces which exist between the nanoparticles and high surface area.[47] The magnetic nature of nanoparticles is responsible for magnetic dipolar interactions.[48] rGO sheets are attached with one another with the help of $\pi-\pi$ interactions.[49] The average size of the CF nanoparticles of RGCF is observed as 16.5 nm. The presence of rGO can also be deduced from the EDXS data (Figure 3c), as attached with the FESEM images. The EDX data in Figure 3c clearly show the elemental existence of C, Co, and Fe as 9.30, 30.41, and 60.30 by weight percent, respectively. The presence of carbon in the EDX patterns corresponds to rGO present in RGCF, and the rest of the elements like Fe and Co contribute to the spinel phase of cobalt ferrite nanoparticles.

The absence of any other peak simply illustrates the sample without impurity. The surface composition of RGCF is further confirmed by elemental mapping (Figure 3g–i). The absence of continuous rGO sheets in the surface composition of RGCF is due to the low quantity of rGO in the composite, which is clear with the carbon percentage present in the sample. The

https://doi.org/10.1021/acsomega.2c06636
ACS Omega 2023, 8, 6376–6390

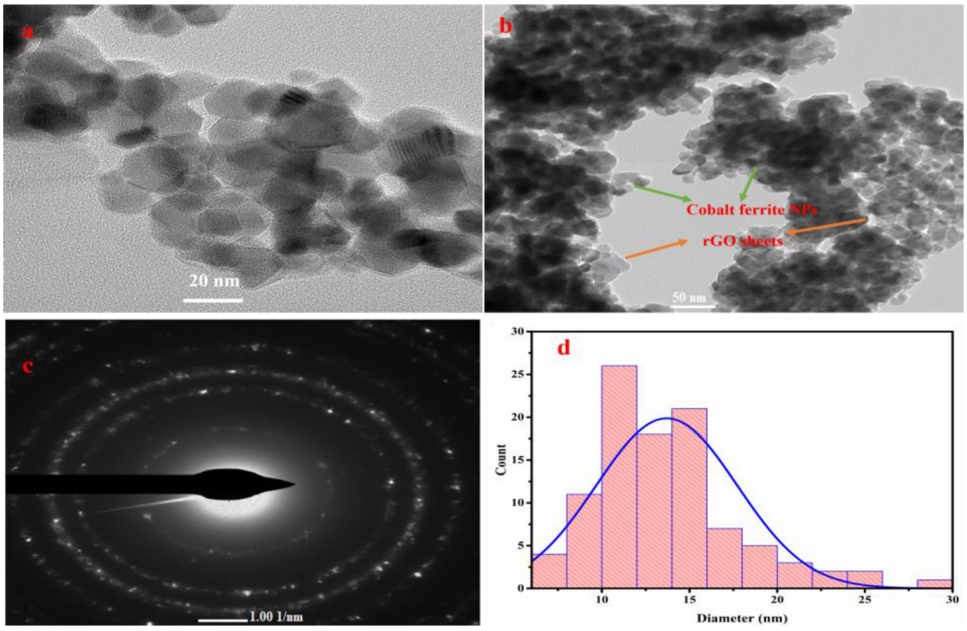

Figure 4. TEM images of the RGCF nanocomposite with 20 nm resolution (a), 50 nm resolution (b), SAED pattern (c), and particle size distribution (d).

SEM micrographs in Figure 3d,e show cloudy lumps all over RGCF, which could be ascribed to the presence of adsorbed dye molecules, which is also evident from the EDX analysis of used RGCF (Figure 3f). The presence of nitrogen in the EDX pattern of used RGCF shows nitrogen of the azo bond present in the dye molecules.

3.1.3.2. TEM Analysis. The morphology and structural analyses were further elaborated for better resolution with the help of TEM images. They reveal the spherical shape of cobalt ferrite, as also confirmed by the FESEM study. rGO sheets could be seen beneath the particles of cobalt ferrite nanoparticles. The RGCF nanocomposite shows the nanosheets of rGO embellished with $CoFe_2O_4$ nanoparticles of smaller size. The intimate relation between rGO sheets and the NPs of $CoFe_2O_4$ limits the aggregation of $CoFe_2O_4$ NPs.[50] The average particle size (Figure 4a) has been calculated as 17.8 nm (the value is close to that obtained by FESEM) by drawing the particle size distribution histogram (Figure 4d) using imageJ software.[51] The SAED pattern in Figure 4c shows all the respective lattices of crystals, proving the polycrystalline nature of RGCF. The respective lattices can be indexed to the FCC structure of spinel $CoFe_2O_4$. The results of TEM were found to be in good agreement with that of XRD.

3.1.4. VSM Measurement. The magnetic property of an adsorbent plays a significant role in the recovery of the adsorbent from the treated waste pollutants. To check the magnetic behavior, vibration sample magnetometer (VSM) measurement has been conducted at room temperature under a strong magnetic field of 20 k Oe. The M−H curve for the synthesized RGCF nanocomposite has been plotted to show the dependency of magnetization on the applied magnetic field. Figure 5 shows the values of saturation magnetization (M_s), remanence/retentivity (M_r), and coercivity (H_c) of RGCF as 23.622 emu/g, 9.4023 emu/g, and 1575 Oe, respectively. The saturation magnetization value obtained is lesser as compared to the bulk (~80 emu/g) due to the magnetic moment distortions present on the surface of nanoparticles.[52] The presence of rGO sheets along with the

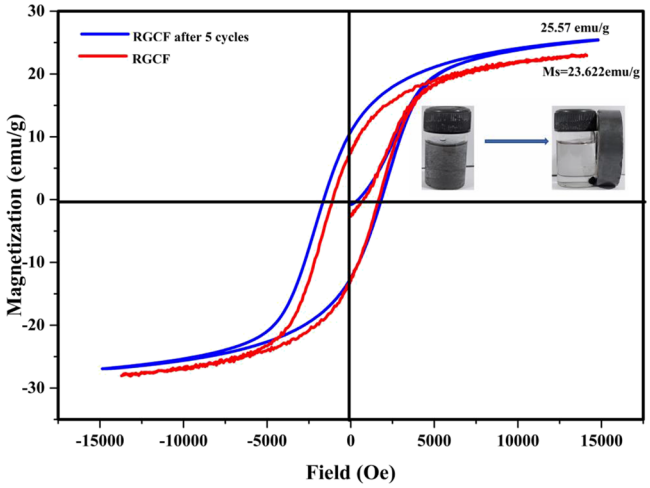

Figure 5. Room-temperature $M-H$ curve for fresh RGCF nanocomposite and after five cycles (inset: magnetic separation).

nanoparticles could be another prime cause for the reduction of magnetic saturation as it further decreases the magnetic dipole interaction among adjacent magnetic particles. The value of saturation magnetization showed a slight variation after use in five consecutive cycles. The variation may be because of the following reasons:

(i) Reduction in the percentage of the carbonaceous material.
(ii) After MO adsorption onto RGCF, the number of oxygen-containing functional groups (SO_3^-) gets increased on the surface of the RGCF composite, thereby increasing the magnetization value by 1.95 emu/g of the dye-doped composite. Even after washing the composite for the regeneration study, there is a chance that some moieties of the MO dye remain intact in the RGCF composite. Thus, it may increase the magnetization value of the washed composite.[53]
(iii) Some instrumental or user handling error.

https://doi.org/10.1021/acsomega.2c06636
ACS Omega 2023, 8, 6376−6390

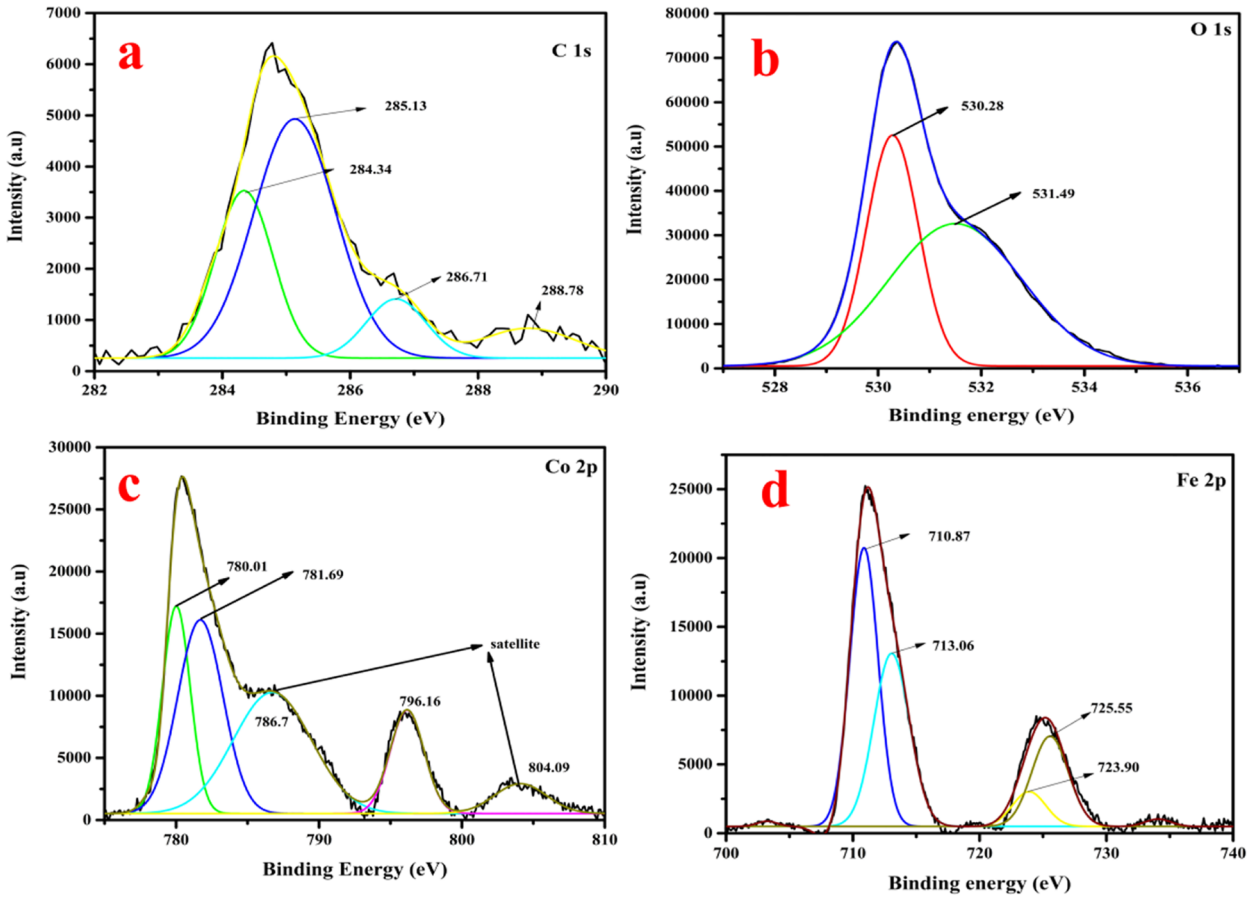

Figure 6. XPS spectra of fresh RGCF nanocomposite: (a) C 1s, (b) O 1s, (c) Co 2p, and (d) Fe 2p.

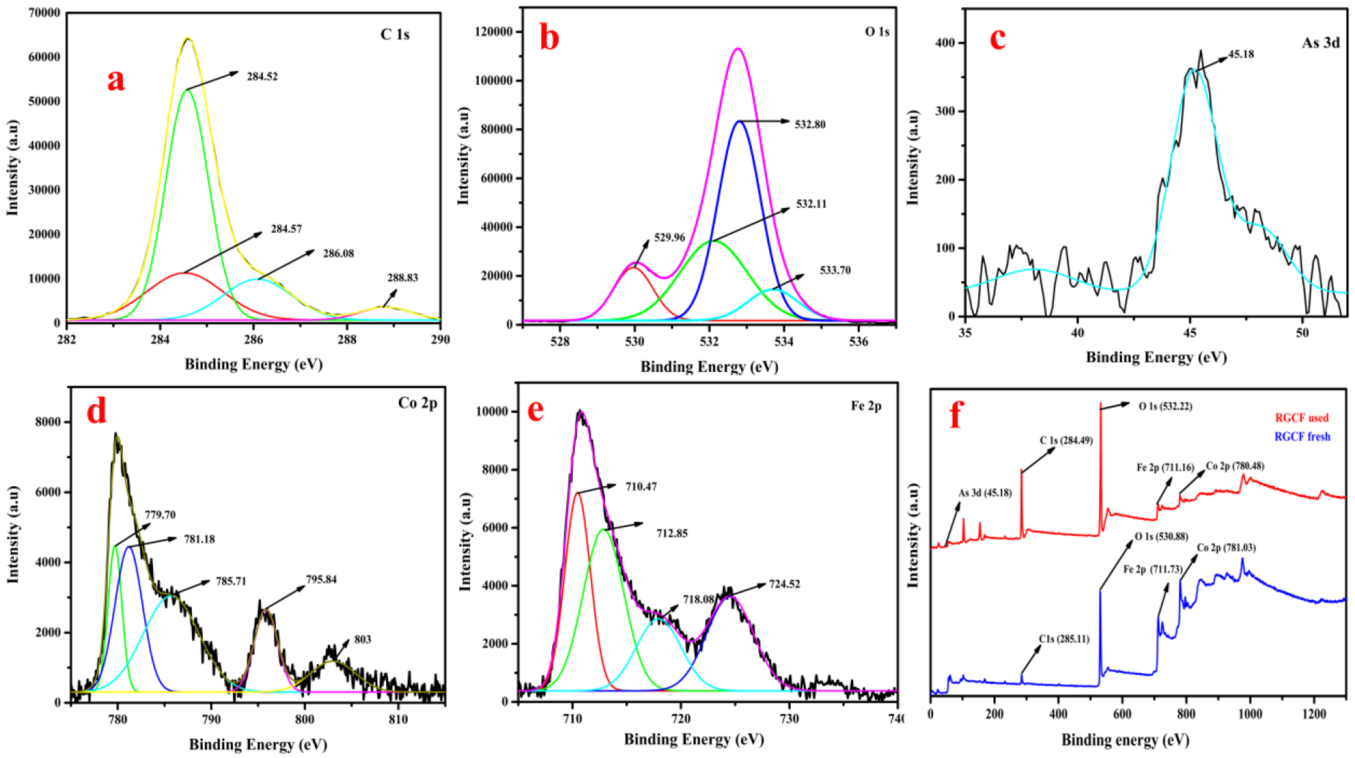

Figure 7. XPS spectra of As-loaded RGCF nanocomposite: (a) C 1s, (b) O 1s, (c) As 3d, (d) Co 2p, and (e) Fe 2p and (f) XPS survey of fresh and used RGCF nanocomposites.

https://doi.org/10.1021/acsomega.2c06636
ACS Omega 2023, 8, 6376−6390

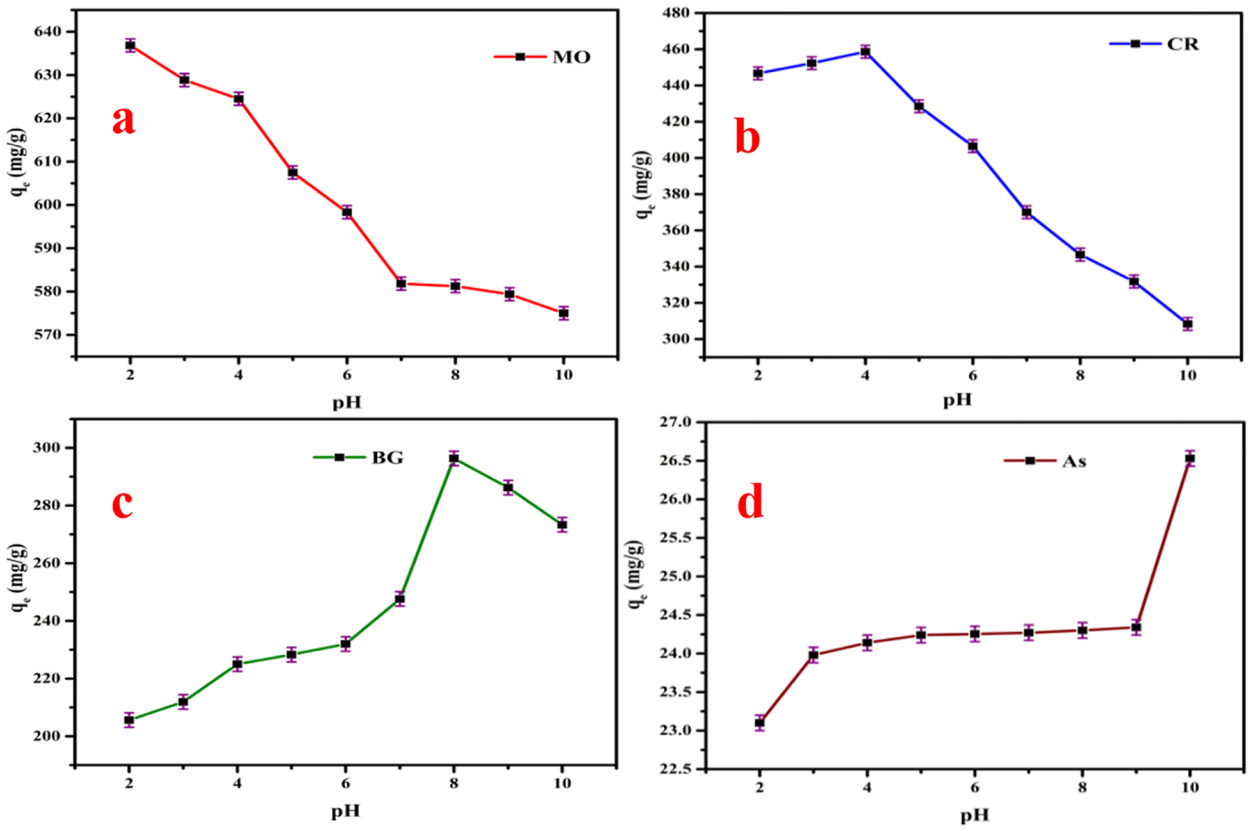

Figure 8. Effect of pH on the adsorption of MO (a), CR (b), BG (c), and As (d) on the RGCF nanocomposite (concentration = 50 mg/L (MO); 30 mg/L (CR); 20 mg/L (BG); 10 mg/L (As); dose = 1.5 mg (MO, CR, and BG); 7 mg (As)); volume = 25 mL (MO, CR, BG, and As); temperature = 298 K).

The value of the obtained saturation magnetization was found enough to show magnetism in the composite as well as for separation from the aqueous medium. The ratio of M_r/M_s was obtained as 39.8%. This value of saturation magnetization is strong enough to consider any material to be superparamagnetic.[20,54]

3.1.5. XPS Measurement. XPS investigates the chemical state of the element and the surface composition of the RGCF nanocomposite. In the XPS survey graph in Figure 6b, the presence of C, O, Co, and Fe in fresh RGCF shows desirable peaks. However, in the As-adsorbed RGCF survey, an extra peak of As(V) ion is present other than C, O, Co, and Fe, which proves the adsorption of arsenate ion over the RGCF adsorbent. There are two main peaks depicted in Figure 6d at 710.87 and 723.90 eV for Fe $2p_{3/2}$ and Fe $2p_{1/2}$, respectively, which are due to the contributions of Fe^{+3} ions at the octahedral (A) sites of the spinel cobalt ferrite. The two peaks at 713.06 and 725.55 eV are called satellite peaks for Fe $2p_{3/2}$ and Fe $2p_{1/2}$ which are due to the contributions of Fe^{+3} ions at the tetrahedral (B) sites. The spectrum of Co 2p (Figure 6c) is found to be similar to that of Fe 2p, as the peaks present at 780.01 and 796.16 eV can be ascribed to Co $2p_{3/2}$ and Co $2p_{1/2}$, respectively, of Co^{+2} ions present at the octahedral sites. However, the peaks at 781.69 eV could be assigned to Co 2p3/2 at the tetrahedral sites of Co^{+2} ions. Additionally, there are two peaks observed at 786.7 and 804.09 eV, which could be ascribed as satellite peaks. The presence of satellite peaks confirms large numbers of high-spin Co^{+2} ions occupying the octahedral sites.[36]

Furthermore, the C 1s spectra of RGCF (Figure 6a) in the deconvoluted form confirm the presence of C═C/C−C (284.34 eV), oxygen-containing groups C−OH (285.13 eV), C−O (286.7 eV), and O−C═O/O−C−O (288.7 eV).[55] The XPS spectrum of O 1s (Figure 6b) shows a peak at 530.28 eV, which corresponds to the oxygen-containing functional groups, while the peak present at 531.49 eV corresponds to the metal oxygen bond (Co−O−Fe). Thus, the result displays the successful formation of the RGCF nanocomposite. However, Figure 7a−e shows separate peaks of parent elements along with adsorbed arsenic onto the RGCF nanocomposite. While comparing the survey graphs of fresh and used RGCF (Figure 7f), it could be clearly demonstrated that there is a reduction in the binding energies of the respective elements. The XPS spectrum of arsenic (As 3d) in Figure 7c shows a peak at 45.18, which clearly shows the presence of As(V) ions from $HAsO_4^{2-}$ species.[56] In Figure 7b, the O 1s spectra show four deconvoluted peaks at 529.96, 532.11, 532.80, and 533.70 eV. The peak at 533.70 eV corresponds to the M−O−M bond, and the rest of the three peaks refer to the functional groups. When comparing the O 1s spectra of fresh and spent RGCF, a slight increase in the number of peaks and binding energies is observed, which is due to the contribution of oxygen from arsenic oxide or interaction of As(V) ion with the adsorbent with the help of M−O and M−OH linkages.[57]

4. ADSORPTION EXPERIMENTS

4.1. Dye Selectivity Tests. To analyze the dye selectivity tests, cationic (CV and BG) and anionic dyes (MO and CR) were taken. All the batch adsorption studies were conducted in

https://doi.org/10.1021/acsomega.2c06636
ACS Omega 2023, 8, 6376−6390

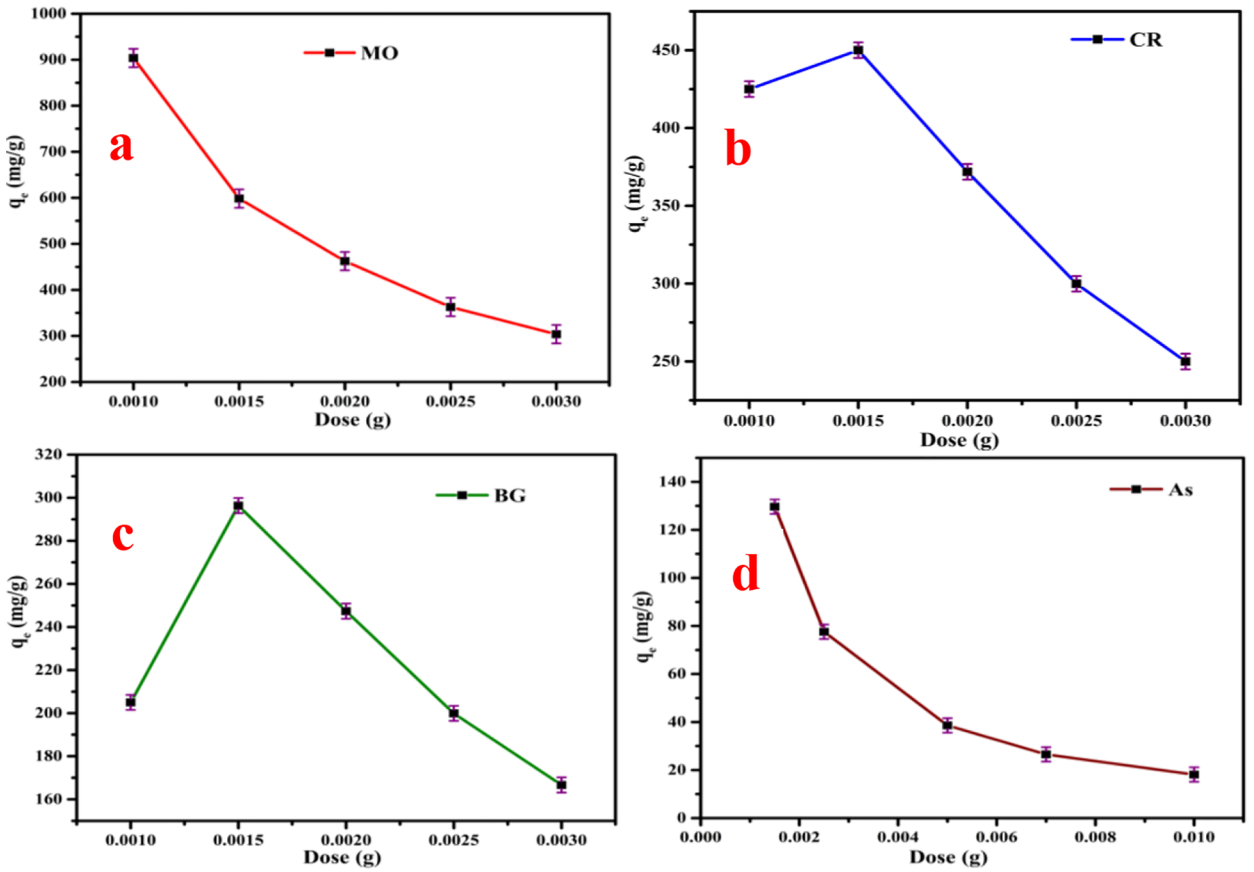

Figure 9. Effect of the adsorbent dose on the amount of MO (a), CR (b), BG (c), and As (d) uptake with the RGCF nanocomposite (concentration = 50 mg/L (MO), 30 mg/L (CR), 20 mg/L (BG), and 10 mg/L (As); pH = 2 (MO), 4 (CR), 8 (BG), and 10 (As); volume = 25 mL (MO, CR, BG, and As); temperature = 298 K).

a series of Erlenmeyer flasks containing 25 mL of model dyes (CV, MO, BG, and CR) and heavy metal (As) solutions under continuous stirring at temperatures of 25 ± 5 °C. In a typical experiment, 0.0015 g of RGCF was taken in a 100 mL Erlenmeyer flask that contains 25 mL of dyes with different concentrations under pH in the range of 2−8. The pH was adjusted by using 0.1 M NaOH or 0.1 M HCl. The dose of the adsorbent was taken from 1 to 10 mg. After optimizing the pH and the dose, isotherm experiments were done in the concentration range of 10−160 mg/L. To determine the kinetics of the reaction, the adsorption capacity was analyzed at different time intervals. Experiments with different parameters were performed on a rotary flask shaker at a constant speed of 150 rpm at 298 K. As soon as equilibrium was achieved, the maximum uptake of dyes occurs. RGCF was separated from the mixture with a handheld magnet. The residual concentrations of the dyes and heavy metal were determined using a UV−vis spectrophotometer and an ICP-OES unit, respectively. The maximum adsorption takes place at λ_{max} of 460, 492, 625, and 588 nm for MO, CR, BG, and CV, respectively. The fraction of dyes adsorbed q_e (mg/g) and removal efficiency (R %) were determined using the following formulas

$$R\% = \frac{C_o - C_t}{C_o} \times 100 \quad (2)$$

$$q_e = \frac{C_o - C_t}{m} \times V \quad (3)$$

where R% is the removal efficiency of the dyes, C_o (mg/L) is the initial concentration of the dyes, C_t (mg/L) is the concentration of the dyes at any time, q (mg/g) is the amount of dye adsorbed per unit amount of adsorbent, V (L) is the volume of the adsorbate, and m (g) is the mass of the adsorbent.

4.2. Effect of pH. pH of the adsorbate solution is considered a significant controlling feature in the adsorption process as it influences the extent of ionization and residual surface charge on the adsorbent.[58] To know the surface charge on the RGCF adsorbent, zeta potential measurement was done. The zeta potential distribution graph (Figure S5) shows the mean data as −7.16 mV charge potential on the surface of RGCF. From the literature, it has been noted that the lower negative or positive value of zeta potential shows a highly unstable form, thereby species tend to attract opposite charges. Further, zeta potential is considered the measurement of the magnitude of surface charge.[59,60] In our case, the surface charge of RGCF in the form of zeta potential is noted negative. The adsorption of dyes and heavy metals onto the RGCF surface was influenced by both initial pH and the surface charge which resides on the adsorbent.[10] The effect of pH on the sorption of RGCF toward dyes and heavy metals was investigated by taking 10 mg/L of As, 50 mg/L of MO, 10 mg/L of CR, and 50 mg/L of BG at different initial pH values under shaking condition. The concentrations of As and dyes were measured after magnetic separation. Figure 8a−d indicates different trends for the removal of cationic and anionic dyes and heavy metals. Cationic dye (BG) was found

https://doi.org/10.1021/acsomega.2c06636
ACS Omega 2023, 8, 6376−6390

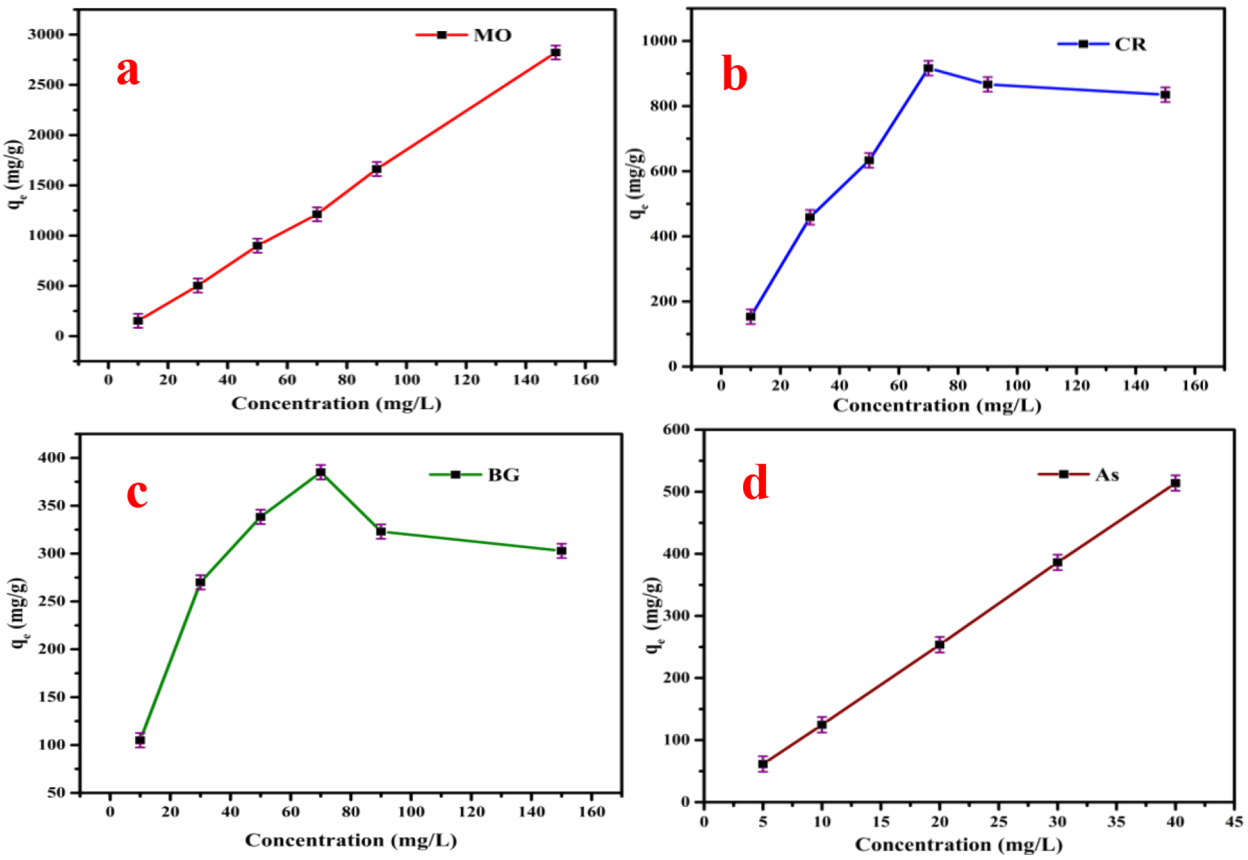

Figure 10. Effect of different initial concentrations of MO (a), CR (b), BG (c), and As (d) for the removal of MO, CR, BG, and As by the RGCF nanocomposite (pH = 2 (MO), 4 (CR), 8 (BG), and 10 (As); dose = 1 mg (MO) and 1.5 mg (CR, BG, and As); volume = 25 mL (MO, CR, BG, and As); and temperature = 298 K).

to be adsorbed at basic pH (above 8), while anionic dye shows removal at acidic pH (between 2 and 4). Arsenic ion removal has been shown at pH 10. At lower pH (2−4), the surface of the adsorbent was highly protonated. Hence, the adsorption of anionic dyes becomes advantageous.

Thus, the obvious reason for the increasing adsorption capacity is the electrostatic attraction forces between the positive surface charge (due to protonation) of RGCF and the anionic species of dye molecules. Further, in cationic dyes and arsenic ions, the adsorption capacity is found to increase with the increasing pH of the solution (pH > 7). The attractive forces between the negative surface of RGCF and the charges of heavy metals and cationic dyes have been discussed in Section 4.7. The data presented in this study illustrate the best adsorption of CR and MO at pH 4 and 2, respectively, while the best adsorption of BG and As was observed at pH 8 and 10, respectively.

4.3. Effect of Adsorbent Dose. Next to pH, the dose of the adsorbent is utmost crucial to be measured to find the optimum value. The effectiveness and adsorption quantity with a minimum dose are important from the economical point of view. The adsorption of MO, CR, BG, and As was carried out by using various doses of RGCF. The adsorbent dose was 0.001 to 0.003 g for MO, CR, and BG dyes and 0.0015 to 0.010 g for As, keeping the rest of the parameters constant in a 100 mL Erlenmeyer flask containing 25 mL of aqueous solution. The graph of adsorption capacity at equilibrium (q_e; mg/g) versus the adsorbent dose (g) has been plotted in Figure 9.

Figure 9a−d shows that the value of q_e continuously decreases from its maximum value as the adsorbent dosage increases in the case of MO and As, while in the case of CR and BG, q_e first increases and then it also follows the decreasing trend with the increasing adsorbent dosage. An increase in the adsorption capacity with increasing dosages was because of the increasing surface area and active functional groups.[61] The decreasing trend after a further increase in dosage suggests the possible agglomeration of RGCF, which ultimately decreases the surface area and increases the diffusion path length.[30]

4.4. Effect of Concentration. To design any adsorption system, pollutant concentration is considered an important parameter. In this study, adsorbent efficiency was evaluated by considering the variable concentrations of dyes and heavy metals, as in Figure 10a−d. Adsorption capacity is seen increasing throughout in the case of MO (Figure 10a) from 10 to 150 mg/L and in As (Figure 10d) from 5 to 40 mg/L, while in the case of CR (Figure 10b), adsorption capacity first increases from 10 to 90 mg/L and then decreases, and in the case of BG (Figure 10c), it increases from 10 to 70 mg/L and then decreases.

The continuous increment in the adsorption capacity of RGCF could be attributed to the increase in the driving force of the concentration gradient with a higher initial dye concentration, or the number of molecules of adsorbate interacting with the available number of sites onto the surface of RGCF nanocomposites increases with the increase in concentration. However, after reaching a certain concentration,

https://doi.org/10.1021/acsomega.2c06636
ACS Omega 2023, 8, 6376−6390

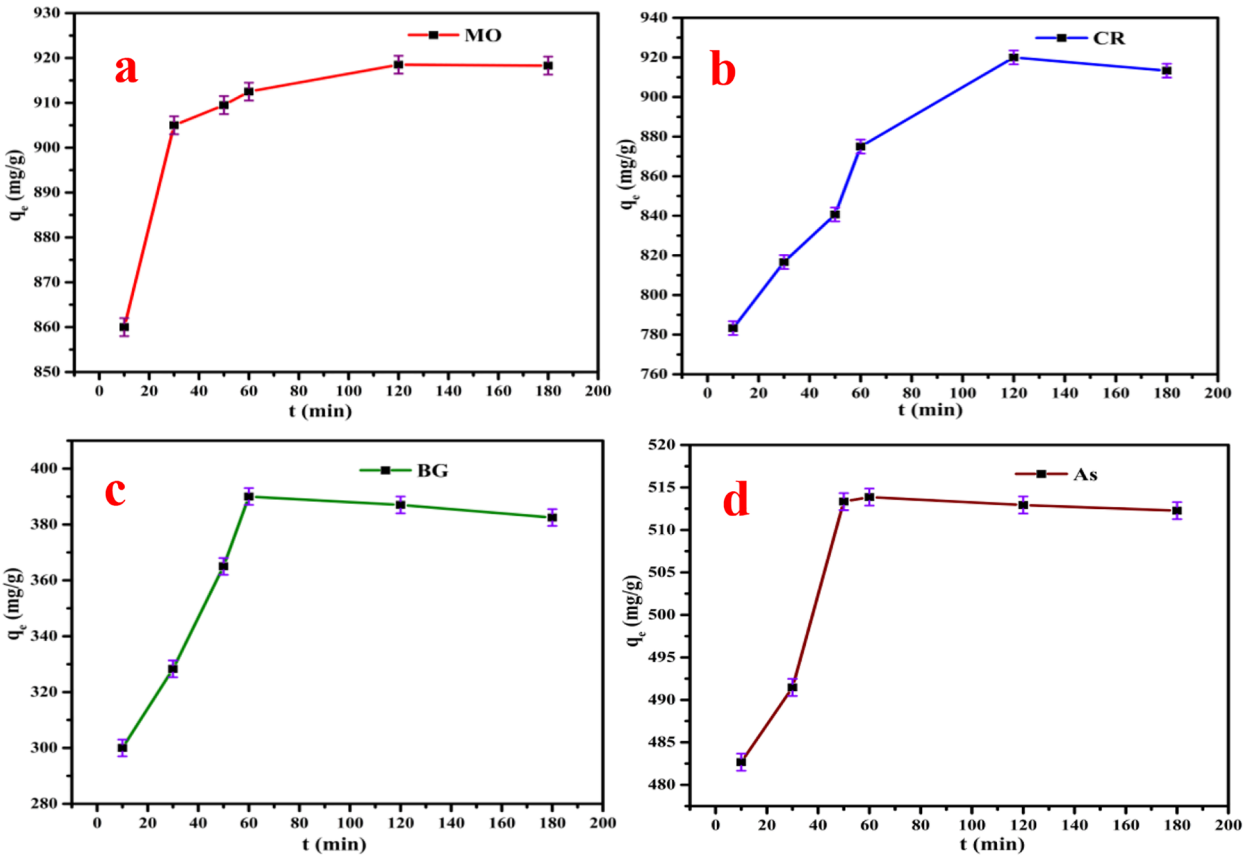

Figure 11. Effect of contact time on the removal of MO (a), CR (b), BG (c), and As (d) by the RGCF nanocomposite (concentration = 150 mg/L (MO), 70 mg/L (CR and BG), and 40 mg/L (As); pH = 2 (MO), 4 (CR), 8 (BG), and 10 (As); dose = 1 mg (MO) and 1.5 mg (CR, BG, and As); volume = 25 mL (MO, CR, BG, and As); and temperature = 298 K).

it decreases because of the further absence of active sites onto the RGCF adsorbent.[62]

4.5. Effect of Time. The effect of contact time for MO, CR, BG, and As has been analyzed from 10 to 180 min by keeping all other parameters in optimized conditions onto the surface of RGCF, as shown in Figure 11. At first, the adsorption capacity increases from 10 to 120 min for MO (860 to 918 mg/g) and CR (783 to 913 mg/g) (Figure 11a,b); 10–60 min for BG and As (Figure 11c,d), and thereafter it either decreases or remains constant. The increase in the adsorbate uptake is due to the vacant surficial active sites onto the RGCF. Later, the adsorption capacity decreases or becomes constant, which is due to the exhaustion of all the active sites of RGCF. The maximum q_e shows that the dyes and heavy metal uptake reached the equilibrium state.[10]

4.6. Adsorption Kinetic Experiments. To design a fast and effective adsorption model, kinetic investigation of any chemical activity is inevitable. Adsorption kinetics is helpful in defining the adsorption mechanism and rate at which it moves toward equilibrium. Kinetic experiments are usually interpreted using pseudo-first-order (PFO) and pseudo-second-order (PSO) models, which are shown by eqs 4 and 5, respectively. The adsorption kinetics of MO, CR, BG, and As onto RGCF have also been investigated using Lagergren pseudo-first-order, pseudo-second-order, intraparticle diffusion, and Elovich models. The linear equations of these models are given below.

(i) (i) Lagergren pseudo-first-order equation[33]

$$\ln(q_e - q_t) = \ln q_e - k_1 t \tag{4}$$

(ii) pseudo-second-order equation[19]

$$\frac{t}{q_t} = \frac{1}{k_2 q_e^2} + \frac{1}{q_e} t \tag{5}$$

(iii) intraparticle diffusion equation[63]

$$q_t = k_i t^{0.5} + C \tag{6}$$

(iv) Elovich equation[63]

$$q_t = \frac{1}{\beta}\ln(\alpha\beta) + \frac{1}{\beta}\ln t \tag{7}$$

where q_e and q_t represent the amount of MO, CR, BG, and As adsorbed (mg/g) onto RGCF at equilibrium and at time t (min), respectively. q_e^{cal} (mg/g) shows the calculated adsorption capacity. K_1 and K_2 represent the pseudo-first-order and pseudo-second-order adsorption rate constants, respectively. K_i is the intraparticle diffusion rate constant. α is the initial adsorption rate (mg g^{-1} min), and β is the number of sites available for adsorption. In the PFO kinetic model, it is considered that one adsorption site occupies one adsorbate molecule, while two adsorption sites are occupied by two adsorbate molecules.[64] The result of kinetic parameters and kinetic models have been displayed in Table S1 and Figure S6a–d, respectively. The value of regression coefficient (r^2) for MO is 1 and 0.99 for CR, BG, and As in the case of PSO model. Hence, the adsorption data could be well simulated by the PSO kinetic model for the RGCF nanocomposite. Furthermore, for all dyes, q_e^{cal} and q_e^{exp} have a close value

https://doi.org/10.1021/acsomega.2c06636
ACS Omega 2023, 8, 6376–6390

for the PSO model which shows chemisorption as the rate-determining step.[10,65] Thus, the adsorption of all dyes along with the heavy metal are governed by PSO model kinetics.

4.7. Adsorption Isotherm Experiments. Adsorption isotherm models: Langmuir and Freundlich models give information about the amount of adsorbent required to remove a unit mass of pollutant under the same conditions. These models are also used to discriminate if the adsorption process is homogeneous (monolayer) or heterogeneous (multilayer). The Langmuir isotherm model describes about the monolayer adsorption which means the monolayer coverage of the adsorbate onto the uniform surface of the adsorbent bearing equivalent adsorption sites. The Freundlich isotherm model could usually be surfaced on multilayers. The equations for the Langmuir, Freundlich, Temkin, and Dubinin−Radushkevich isotherm models can be written as follows

$$C_e q_e = C_e q_m + \frac{1}{K_L q_m} \tag{8}$$

$$\log q_e = \log K_F + \frac{1}{n}\log C_e \tag{9}$$

$$q_e = \frac{RT}{b}\ln A + \frac{RT}{b}\ln C_e \tag{10}$$

$$B_T = RT/b$$

$$\ln q_e = \ln q_{DR} - K_{DR}\varepsilon^2 \tag{11}$$

where C_e and q_e are the equilibrium concentration (mg/L) and equilibrium adsorption capacity (mg/g), respectively. q_m is the maximum value of adsorption capacity by a single-layer adsorbent surface. The linear curve of the Langmuir equation has been plotted against $1/q_e$ and $1/C_e$, which determines the magnitude of q_m and K_L. K_L and K_F are the Langmuir and Freundlich constants in (L mg^{-1}) and [(mg g^{-1}) (L $mg^{-1})^{1/n}$, respectively. A dimensionless Langmuir parameter R_L (separation factor) is used to know whether the adsorption process is favorable or not. R_L is the measure of affinity between the adsorbent and adsorbate. Adsorption is considered to occur if the value of $R_L > 0$.[60] The values of R_L (Table S1) are found for MO (0.337423), CR (0.057873), BG (0.132679), and As (0.084435). It clearly validates the favorable conditions of adsorption of MO, CR, BG, and As onto the RGCF nanocomposite. K_F values as obtained from eq 9 indicate the high uptake of adsorbate onto the RGCF nanocomposite. The linear fitting curve for log C_e versus log q_e has been plotted to find the multilayer coverage (Freundlich isotherm model). All the related parameters for MO, CR, BG, and As observed from the Langmuir, Freundlich, Temkin, and Dubinin−Radushkevich isotherms have been shown in Table S1. The linear fitting for Temkin and Dubinin−Radushkevich isotherms has also been studied (Figure S7c,d. A_T (eq 10) is the Temkin isotherm equilibrium binding constant (Lg^{-1}), q_{DR} is the theoretical isotherm saturation capacity (mg/g), and K_{DR} is the Dubinin−Radushkevich isotherm constant (mol^2 kJ^{-2}). Based on the value of higher correlation coefficient (r^2), the Langmuir model resonates well with the adsorption of all dyes and the heavy metal onto the surface of the RGCF nanocomposite, that is, the physical intermolecular attraction between the adsorbent and adsorbate is predominated. Thus, this indicates the monolayer coverage and homogeneous distribution of the adsorbate on the adsorbent surface. The maximum adsorption capacity (q_m) from Figure S6a for MO, CR, BG, and As was found to be 1666.67, 1000, 416.6, and 222.23 mg/g, respectively. It has been recorded that the maximum adsorption capacity of the RGCF nanocomposite is better as compared to other reported adsorbents (Table S3).

4.8. Thermodynamic Study. To analyze the temperature effect on the adsorption process, parameters like Gibbs energy (ΔG), entropy (ΔS), and enthalpy (ΔH) have been studied using eqs 12 and 13[66]

$$\Delta G = -RT\ln K_c \tag{12}$$

$$\ln K_c = \frac{\Delta S}{R} - \frac{\Delta H}{RT} \tag{13}$$

where R (8.314 J/mol K) is the gas constant, T (K) is the absolute temperature, and K_c is known as the equilibrium partition coefficient. K_c can be further calculated from eq 14[66]

$$K_c = \frac{q_e}{C_e} \tag{14}$$

where q_e is the adsorption capacity in mg/g of the dyes and heavy metal at equilibrium time. C_e is the equilibrium concentration in mg/L of the dyes and heavy metal solution. The change in enthalpy (ΔH) and change in entropy (ΔS) can be found from the slope and intercept values, respectively, using the linear plot of ln K_c versus $1/T$. Table S2 represents the calculated data. The assessment of thermodynamic parameters has been done in a batch system to find out the MO, CR, BG, and As uptake from an aqueous solution at varying temperatures of 298.15, 308.15, 318.5, and 328.5 K with the previously optimized conditions using the RGCF nanocomposite (Figure S8). As per the data figured in Table S2, ΔG^0 values for MO, CR, BG, and As are found negative, which manifests the spontaneity and feasibility of the adsorption process. A positive value of ΔS^0 shows an increase in randomness during the adsorption of dyes and heavy metals onto the RGCF nanocomposite. The value of ΔH^0 implies the endothermic nature of the adsorption process.[66] The values of ΔG^0 and ΔH^0 are less than −20 kJ and 40 kJ/mol, respectively, referring to the physisorption between the adsorbate and adsorbent surface.

4.9. Adsorption Mechanism Study. Dye adsorption mechanism could be controlled by various physical and chemical factors of adsorbents. It is a well-known fact that the surface of rGO bears many negative functional groups and aromatic rings. It is therefore capable of dye adsorption via electrostatic interaction, $\pi-\pi$ conjugation, and H bonding. The homogeneous distribution of $CoFe_2O_4$ nanoparticle onto rGO provides sufficient surface area and surface functionalities.[67] In our study, the surface of RGCF is known to be negatively charged (zeta potential of −7.16 mV in water at pH 7 (Figure S5). The protonation and deprotonation processes produce different charges due to the pH maintenance. Thus, electrostatic attraction plays a major role in the removal of dyes along with $\pi-\pi$ interaction and H bonding.[9,68] Both MO and CR are anionic azo dyes which contain the sulfonic acid groups. Intense FTIR peaks at 1050 and 1162 cm^{-1} on CR-loaded RGCF (Figure S1b) and at 1114 cm^{-1} on MO-loaded RGCF (Figure S1c) show electrostatic attraction forces between the stretching and bending vibrations of sulfonate anions and OH_2^+ of graphene sheets (at working pH). Hence, an electrostatic force may exist between the sulfonate anions

https://doi.org/10.1021/acsomega.2c06636
ACS Omega 2023, 8, 6376−6390

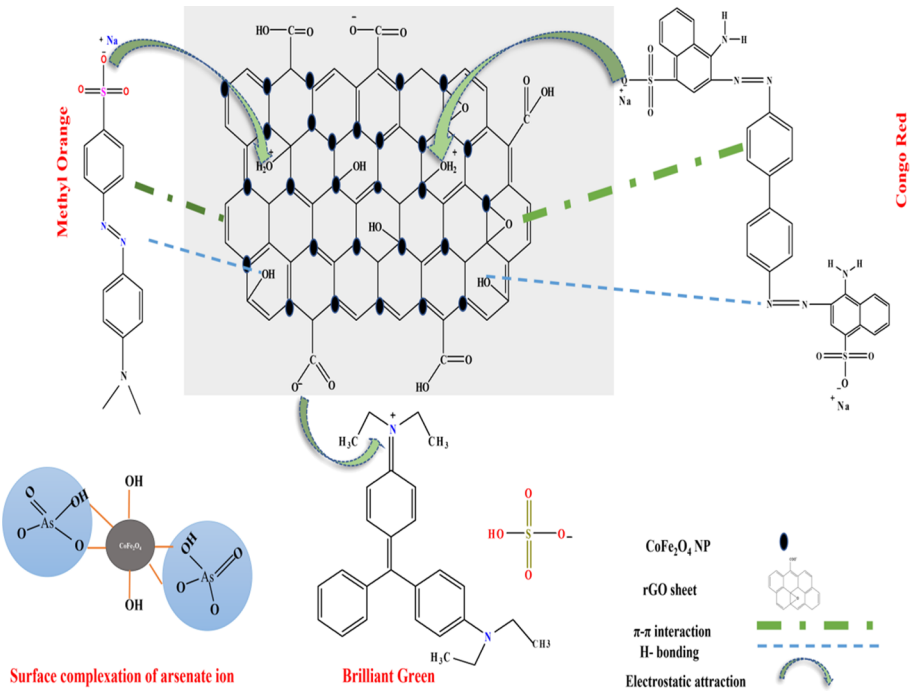

Figure 12. Adsorption mechanism of MO, CR, BG, and arsenic with the RGCF nanocomposite.

($R-SO_3^-$) and the surface of RGCF. As per previous literature reports,[69] the π electrons of the aromatic ring of rGO along with the π electrons of the aromatic ring of azo dyes (MO and CR) may form $\pi-\pi$ interactions. As per the obtained data, best adsorption was found at pH 2 and 4 for MO and CR, respectively, as the RGCF surface attains a positive charge at the working pH of 2 and 4 due to protonation. At the working pH of 10, the negatively charged RGCF surface further attains more negative charges. Therefore, there is an electrostatic attraction between the cationic dye BG and the surface of RGCF. As dyes are usually highly constituted by conjugated systems, aromatic interactions such as $\pi-\pi$ stacking could be well observed. The abundant oxy and hydroxy groups present on the RGCF surface bind with the amine group of dyes via hydrogen bonding.[40]

To know the adsorption mechanism of arsenic ions (arsenate), an XPS study has been conducted and studied. During the course of As(V) adsorption onto the surface of RGCF, there has been considerable shifting in the binding energies of all elements (Figure 7a–e). The deconvolution of O 1s (Figure 7b) results in four peaks in As-loaded RGCF, which shows a change in the percentage of oxygen. The percentage of surface hydroxyl groups increased with the decrease in surface oxygen O_2^- following As adsorption, as seen by the O 1s peak at 529.96 eV. The surface of RGCF after adsorption became hydroxylated, probably due to the formation of highly hydroxylated arsenate complexes. The literature suggests that the predominant species of arsenic is present in the form of $HAsO_4^{2-}$ or AsO_4^{3-} at higher pH (6–12). Hence, the experiment of arsenic adsorption was conducted in the pH range of 2–11. From Figure 8, it is observed that the maximum adsorption has taken place at a higher pH (10). Thus, the probable mechanism involved in adsorption of arsenic was in the form of anionic arsenic ions ($HAsO_4^{2-}$) on the RGCF nanocomposite. Usually, the complex formation and electrostatic interaction are associated with the adsorption of As ions. From Figure 12, it is observed that the surface complexation of $HAsO_4^{2-}$ on the surface of cobalt ferrite nanoparticles takes place via the formation of an inner sphere complex between the surface metal centers As–O–M (M = Fe/Co) and arsenic acid moieties. The hydroxyl groups situated on the surface of cobalt iron oxide and the As–O(H) groups from the arsenate species together undergo ligand exchange reactions, which finally form an inner sphere complex. Thus, the adsorption mechanism of As(V) suggests that the surface complexation reaction may be responsible for the adsorption onto the surface of the RGCF nanocomposite.[56,57]

4.10. Desorption and Regeneration Study. Desorption and regeneration studies are considered quite important to find out the commercial applicability of any adsorbent. To find out the feasibility of the RGCF nanocomposite to be reused, desorption and regeneration studies have been carried out. For this, 0.005 g adsorbent was used with 70 mg/L of MO, CR, and BG dyes and arsenic solution. The dye- and arsenic-loaded RGCF has been desorbed using ethyl alcohol and deionized water. The dye- and arsenic-saturated RGCF was immersed in ethyl alcohol and water for 12 h at room temperature. After three to four times of consecutive washing with a slightly concentrated NaOH and HCl and then drying, the surface hydroxyl group gets deprotonated, which facilitates the desorption of dyes and arsenic species. Due to strong paramagnetism of the RGCF nanocomposite, it readily separated from the desorb solution by simply placing a magnet which facilitates the reusability.[70] The adsorbent has been found to be reusable up to five consecutive cycles with good adsorption capacity. The reusability tests have been conducted using the abovementioned parameters, and the number of cycles along with their adsorption capacity has been shown in Figure S3.

https://doi.org/10.1021/acsomega.2c06636
ACS Omega 2023, 8, 6376–6390

5. CONCLUSIONS

In this paper, we synthesized the RGCF nanocomposite using a facile chemical precipitation method. The as-synthesized RGCF has a spherical structure of cobalt ferrite nanoparticles with an average diameter of about 10 nm. There is a strong correlation between the adsorption dependency and parameters like the pH of the solution, the RGCF dosage, and the adsorbate concentration. There was a maximum adsorption of MO and CR (anionic species) at pH 2 and 4, respectively, while BG and As had a maximum adsorption at pH 8 and 10, respectively. RGCF displays a much higher adsorption capacity for both anionic and cationic dyes and the heavy metal (As), owing to electrostatic interactions, $\pi-\pi$ interactions, H bonding, and surface complexation between RGCF and dyes/heavy metal. It is evident from the isotherm behavior of RGCF that the adsorption of MO, CR, BG, and As corresponds better to the Langmuir model than the Freundlich model. A comparison with the reported work shows that RGCF exhibits large maximum adsorption rates (q_m) of 1666.7, 1000, 416.6, and 222.2 mg/g, respectively, for MO, CR, BG, and As at 298 K. Moreover, the uptake of MO, CR, BG, and As suggests a pseudo-second-order model, confirming chemisorption as the rate-determining mechanism. The thermodynamic parameters further reveal that the adsorption of dyes MO, CR, and BG, as well as the As metal, spontaneously onto the RGCF nanocomposite is endothermic and thermodynamically stable. It was found from the VSM study that RGCF exhibits strong superparamagnetic behavior, which makes it easy for them to be recovered from solutions with the help of a magnet. As a result of the five-cycle adsorption−desorption process, their adsorption capacity slightly decreases. Consequently, the magnetic nature of metal oxide (cobalt ferrite) combined with a larger surface area of rGO enables the creation of a nanocomposite which is both easy to separate and reusable with ample space for adsorption. Thus, the application of the RGCF nanocomposite for the removal of various dyes and heavy metals is shown to be quite promising.

■ ASSOCIATED CONTENT

Supporting Information

The Supporting Information is available free of charge at https://pubs.acs.org/doi/10.1021/acsomega.2c06636.

FTIR spectra of the RGCF nanocomposite and the MO-, CR-, BG-, and As-loaded RGCF nanocomposite; MO, CR, and BG dyes before and after adsorption; reusability cycles for the dyes and heavy metal; maximum dye and As adsorption for the RGCF nanocomposite; rGO and cobalt ferrite nanoparticles,; zeta potential measurement of the RGCF nanocomposite at pH 7; graphs and tables for kinetic, isotherm and thermodynamic studies, obtained for the removal of dyes and heavy metal using the RGCF nanocomposite. Comparison table for maximum adsorption capacity obtained for removal of dyes and heavy metals by RGCF nanocomposite with other reported literatures (PDF)

■ AUTHOR INFORMATION

Corresponding Authors

Zafar Iqbal − *Environmental Science Research Lab, Department of Applied Sciences & Humanities, Faculty of Engineering & Technology, Jamia Millia Islamia, New Delhi 110025, India*; orcid.org/0000-0001-9631-487X; Email: zafariqbal.amu88@gmail.com

Masood Alam − *Environmental Science Research Lab, Department of Applied Sciences & Humanities, Faculty of Engineering & Technology, Jamia Millia Islamia, New Delhi 110025, India*; Email: malam@jmi.ac.in

Author

Mohd Saquib Tanweer − *Environmental Science Research Lab, Department of Applied Sciences & Humanities, Faculty of Engineering & Technology, Jamia Millia Islamia, New Delhi 110025, India*; orcid.org/0000-0001-5401-0667

Complete contact information is available at: https://pubs.acs.org/10.1021/acsomega.2c06636

Notes

The authors declare no competing financial interest.

■ ACKNOWLEDGMENTS

One of the authors Zafar Iqbal is thankful to CSIR-HRDG, New Delhi, for the fellowship in the form of SRF-Direct.

■ REFERENCES

(1) Tanweer, M. S.; Alam, M. *Novel 2D Nanomaterial Composites Photocatalysts: Application in Degradation of Water Contaminants*; Springer Nature Singapore, 2022; pp 75−96.

(2) Tanweer, M. S.; Chauhan, H.; Alam, M. *Advanced 2D Nanomaterial Composites: Applications in Adsorption of Water Pollutants and Toxic Gases*, 2022; pp 97−124.

(3) Ahmad, R.; Ansari, K. Enhanced Sequestration of Methylene Blue and Crystal Violet Dye onto Green Synthesis of Pectin Modified Hybrid (Pect/AILP-Kal) Nanocomposite. *Process Biochem.* **2021**, *111*, 132−143.

(4) Ahmad, R.; Ansari, K. Comparative Study for Adsorption of Congo Red and Methylene Blue Dye on Chitosan Modified Hybrid Nanocomposite. *Process Biochem.* **2021**, *108*, 90−102.

(5) Saxena, R.; Saxena, M.; Lochab, A. Recent Progress in Nanomaterials for Adsorptive Removal of Organic Contaminants from Wastewater. *ChemistrySelect* **2020**, *5*, 335−353.

(6) Wu, X.; Wang, W.; Li, F.; Khaimanov, S.; Tsidaeva, N.; Lahoubi, M. PEG-Assisted Hydrothermal Synthesis of CoFe 2 O 4 Nanoparticles with Enhanced Selective Adsorption Properties for Different Dyes. *Appl. Surf. Sci.* **2016**, *389*, 1003−1011.

(7) Li, X.; Lu, H.; Zhang, Y.; He, F.; Jing, L.; He, X.; Li, X.; Lu, H.; Zhang, Y.; He, F.; Jing, L.; He, X. Fabrication of Magnetic Alginate Beads with Uniform Dispersion of CoFe₂O₄ by the Polydopamine Surface Functionalization for Organic Pollutants Removal. *Appl. Surf. Sci.* **2016**, *389*, 567−577.

(8) Litefti, K.; Freire, M. S.; Stitou, M.; González-Álvarez, J. Adsorption of an Anionic Dye (Congo Red) from Aqueous Solutions by Pine Bark. *Sci. Rep.* **2019**, *9*, 16530.

(9) Salem, M. A.; Elsharkawy, R. G.; Hablas, M. F. Adsorption of Brilliant Green Dye by Polyaniline/Silver Nanocomposite: Kinetic, Equilibrium, and Thermodynamic Studies. *Eur. Polym. J.* **2016**, *75*, 577−590.

(10) Tanweer, M. S.; Iqbal, Z.; Alam, M. Experimental Insights into Mesoporous Polyaniline-Based Nanocomposites for Anionic and Cationic Dye Removal. *Langmuir* **2022**, *38*, 8837−8853.

(11) Fu, D.; He, Z.; Su, S.; Xu, B.; Liu, Y.; Zhao, Y. Fabrication of α-FeOOH Decorated Graphene Oxide-Carbon Nanotubes Aerogel and Its Application in Adsorption of Arsenic Species. *J. Colloid Interface Sci.* **2017**, *505*, 105−114.

(12) Mandal, P. An Insight of Environmental Contamination of Arsenic on Animal Health. *Emerging Contam.* **2017**, *3*, 17−22.

(13) Iqbal, Z.; Tanweer, M. S.; Alam, M. Recent Advances in Adsorptive Removal of Wastewater Pollutants by Chemically Modified Metal Oxides: A Review. *J. Water Process Eng.* **2022**, *46*, No. 102641.
(14) Ali, S.; Tanweer, M. S.; Alam, M. Kinetic, Isothermal, Thermodynamic and Adsorption Studies on Mentha Piperita Using ICP-OES. *Surf. Interfaces* **2020**, *19*, No. 100516.
(15) Ikram, M.; Naeem, M.; Zahoor, M.; Mohd Hanafiah, M.; Abdulrahman Oyekanmi, A.; Ullah, R.; Al Farraj, D. A.; Elshikh, M. S.; Zekker, I.; Gulfam, N. Biological Degradation of the Azo Dye Basic Orange 2 by Escherichia Coli: A Sustainable and Ecofriendly Approach for the Treatment of Textile Wastewater. *Water* **2022**, *14*, 2063.
(16) Liu, X.; Chen, Z.; Du, W.; Liu, P.; Zhang, L.; Shi, F. Treatment of Wastewater Containing Methyl Orange Dye by Fluidized Three Dimensional Electrochemical Oxidation Process Integrated with Chemical Oxidation and Adsorption. *J. Environ. Manage.* **2022**, *311*, No. 114775.
(17) de Oliveira, H. A. L.; Campos, A. F. C.; Gomide, G.; Zhang, Y.; Ghoshal, S. Elaboration of a Core@shell Bimagnetic Nanoadsorbent ($CoFe_2O_4$@γ-Fe_2O_3) for the Removal of As(V) from Water. *Colloids Surf., A* **2020**, *600*, No. 125002.
(18) Deng, J.-H.; Zhang, X.-R.; Zeng, G.-M.; Gong, J.-L.; Niu, Q.-Y.; Liang, J. Simultaneous Removal of Cd(II) and Ionic Dyes from Aqueous Solution Using Magnetic Graphene Oxide Nanocomposite as an Adsorbent. *Chem. Eng. J.* **2013**, *226*, 189−200.
(19) Wu, C.; Dong, D.; Yu, X.; He, P.; Zhang, W. Mesoporous Carbon/Cobalt Ferrite Nanocomposite: A Charge and PH Independent Magnetic Adsorbent for Dye Pollutant Treatment. *Diamond Relat. Mater.* **2020**, *105*, No. 107796.
(20) Wei, F.; Wang, H.; Ran, W.; Liu, T.; Liu, X. Preparation of S−N Co-Doped $CoFe_2O_4$@rGO@TiO_2 Nanoparticles and Their Superior UV-Vis Light Photocatalytic Activities. *RSC Adv.* **2019**, *9*, 6152−6162.
(21) Fu, W.; Huang, Z. Magnetic Dithiocarbamate Functionalized Reduced Graphene Oxide for the Removal of Cu(II), Cd(II), Pb(II), and Hg(II) Ions from Aqueous Solution: Synthesis, Adsorption, and Regeneration. *Chemosphere* **2018**, *209*, 449−456.
(22) Kumar, N.; Dwivedi, S. K.; Kumar Dwivedi, S.; Tiwari, C.; Tomar, R. Study of RGO-CNF/Ce-TiO_2 Based Hetrojunction for Optoelectronic Devices. *Mater. Lett.* **2022**, *315*, No. 131945.
(23) Ates, M.; Yildirim, M.; Kuzgun, O.; Ozkan, H. The Synthesis of RGO, RGO/RuO_2 and RGO/RuO_2/PVK Nanocomposites, and Their Supercapacitors. *J. Alloys Compd.* **2019**, *787*, 851.
(24) Mussa, Y.; Ahmed, F.; Arsalan, M.; Alsharaeh, E. Two dimensional (2D) Reduced Graphene Oxide (RGO)/Hexagonal Boron Nitride (h-BN) Based Nanocomposites as Anodes for High Temperature Rechargeable Lithium-Ion Batteries. *Sci. Rep.* **2020**, *10*, 1882.
(25) Lee, K.; Yoo, Y.; Chae, M.; Hwang, K.; Lee, J.; Kim, H.; Hur, D.; Lee, J. H. Highly Selective Reduced Graphene Oxide (RGO) Sensor Based on a Peptide Aptamer Receptor for Detecting Explosives. *Sci. Rep.* **2019**, *9*, 10297.
(26) Vinoth, R.; Babu, S.; Bharti, V.; et al. *Sci. Rep.* **2017**, *7*, 43133.
(27) Robati, D.; Rajabi, M.; Moradi, O.; Najafi, F.; et al. Kinetics and Thermodynamics of Malachite Green Dye Adsorption from Aqueous Solutions on Graphene Oxide and Reduced Graphene Oxide. *J. Mol. Liq.* **2016**, *214*, 259.
(28) Wang, S.; Jiang, S. P.; Wang, X. Microwave-Assisted One-Pot Synthesis of Metal/Metal Oxide Nanoparticles on Graphene and Their Electrochemical Applications. *Electrochim. Acta* **2011**, *56*, 3338−3344.
(29) Behura, R.; Sakthivel, R.; Das, N. Synthesis of Cobalt Ferrite Nanoparticles from Waste Iron Ore Tailings and Spent Lithium Ion Batteries for Photo/Sono-Catalytic Degradation of Congo Red. *Powder Technol.* **2021**, *386*, 519−527.
(30) Yavari, S.; Mahmodi, N. M.; Teymouri, P.; Shahmoradi, B.; Maleki, A. Cobalt Ferrite Nanoparticles: Preparation, Characterization and Anionic Dye Removal Capability. *J. Taiwan Inst. Chem. Eng.* **2016**, *59*, 320−329.
(31) El-Shafai, N. M.; El-Khouly, M. E.; El-Kemary, M.; Ramadan, M. S.; Masoud, M. S. Graphene Oxide−Metal Oxide Nanocomposites: Fabrication, Characterization and Removal of Cationic Rhodamine B Dye. *RSC Adv.* **2018**, *8*, 13323−13332.
(32) Guo, R.; Jiao, T.; Li, R.; Chen, Y.; Guo, W.; Zhang, L.; Zhou, J.; Zhang, Q.; Peng, Q. Sandwiched Fe_3O_4/Carboxylate Graphene Oxide Nanostructures Constructed by Layer-by-Layer Assembly for Highly Efficient and Magnetically Recyclable Dye Removal. *ACS Sustainable Chem. Eng.* **2018**, *6*, 1279−1288.
(33) Ibrahim, S. M.; Badawy, A. A.; Essawy, H. A. Improvement of Dyes Removal from Aqueous Solution by Nanosized Cobalt Ferrite Treated with Humic Acid during Coprecipitation. *J. Nanostruct. Chem.* **2019**, *9*, 281−298.
(34) Du, R.; Cao, H.; Wang, G.; Dou, K.; Tsidaeva, N.; Wang, W. PVP Modified RGO/$CoFe_2O_4$ Magnetic Adsorbents with a Unique Sandwich Structure and Superior Adsorption Performance for Anionic and Cationic Dyes. *Sep. Purif. Technol.* **2022**, *286*, No. 120484.
(35) Jo, J.; Lee, S.; Gim, J.; Song, J.; Kim, S.; Mathew, V.; Alfaruqi, M. H.; Kim, S.; Lim, J.; Kim, J. Facile Synthesis of Reduced Graphene Oxide by Modified Hummer's Method as Anode Material for Li-, Na- and K-Ion Secondary Batteries. *R. Soc. Open Sci.* **2019**, *6*, No. 181978.
(36) Vijayalakshmi, S.; Elanthamilan, E.; Merlin, J. P.; Lydia, I. S. Tuning the Efficiency of $CoFe_2O_4$@rGO Composite by Encapsulating Ag Nanoparticles for the Photocatalytic Degradation of Methyl Violet Dye and Energy Storage Systems. *New J. Chem.* **2021**, *45*, 17642−17653.
(37) Iqbal, Z.; Siddiqui, V. U.; Alam, M.; Siddiqi, W. A. Synthesis of Copper (II) Oxide Nanoparticles by Pulsed Sonoelectrochemical Method and Its Characterization. In *AIP Conference Proceedings*; American Institute of Physics Inc., 2020; Vol. *2276*, p 020010.
(38) Kalam, A.; Al-Sehemi, A. G.; Assiri, M.; Du, G.; Ahmad, T.; Ahmad, I.; Pannipara, M. Modified Solvothermal Synthesis of Cobalt Ferrite ($CoFe_2O_4$) Magnetic Nanoparticles Photocatalysts for Degradation of Methylene Blue with H_2O_2/Visible Light. *Results Phys.* **2018**, *8*, 1046−1053.
(39) Rakshit, R.; Khatun, E.; Pal, M.; Talukdar, S.; Mandal, D.; Saha, P.; Mandal, K. Influence of Functional Group of Dye on the Adsorption Behaviour of $CoFe_2O_4$ Nano-Hollow Spheres. *New J. Chem.* **2017**, *41*, 9095−9102.
(40) Khani, R.; Irani, M. A Reusable Reduced Graphene Oxide-Cobalt Oxide Nanocomposite with Excellent Yield as Adsorbent for Determination Trace-Level of Brilliant Green in Environmental Water Samples. *Res. Chem. Intermed.* **2020**, *46*, 2137−2154.
(41) Asses, N.; Ayed, L.; Hkiri, N.; Hamdi, M. Congo Red Decolorization and Detoxification by Aspergillus Niger: Removal Mechanisms and Dye Degradation Pathway. *Biomed. Res. Int.* **2018**, *2018*, No. 3049686.
(42) Yang, S.; Wang, L.; Zhang, X.; Yang, W.; Song, G. Enhanced Adsorption of Congo Red Dye by Functionalized Carbon Nanotube/Mixed Metal Oxides Nanocomposites Derived from Layered Double Hydroxide Precursor. *Chem. Eng. J.* **2015**, *275*, 315−321.
(43) Bartošová, A.; Blinová, L.; Sirotiak, M.; Michalíková, A. Usage of FTIR-ATR as Non-Destructive Analysis of Selected Toxic Dyes. *Res. Pap. − Fac. Mater. Sci. Technol., Slovak Univ. Technol.* **2017**, *25*, 103−111.
(44) Acemioğlu, B. Adsorption of Congo Red from Aqueous Solution onto Calcium-Rich Fly Ash. *J. Colloid Interface Sci.* **2004**, *274*, 371−379.
(45) Cyril, N.; George, J. B.; Joseph, L.; Sylas, V. P. Catalytic Degradation of Methyl Orange and Selective Sensing of Mercury Ion in Aqueous Solutions Using Green Synthesized Silver Nanoparticles from the Seeds of Derris Trifoliata. *J. Cluster Sci.* **2019**, *30*, 459−468.
(46) Mansour, R. A. E. G.; Simeda, M. G.; Zaatout, A. A. Removal of Brilliant Green Dye from Synthetic Wastewater under Batch Mode Using Chemically Activated Date Pit Carbon. *RSC Adv.* **2021**, *11*, 7851−7861.

https://doi.org/10.1021/acsomega.2c06636
ACS Omega 2023, 8, 6376−6390

(47) Mahdikhah, V.; Saadatkia, S.; Sheibani, S.; Ataie, A. Outstanding Photocatalytic Activity of CoFe2O4/RGO Nanocomposite in Degradation of Organic Dyes. *Opt. Mater.* **2020**, *108*, No. 110193.
(48) Jelokhani, F.; Sheibani, S.; Ataie, A. Adsorption and Photocatalytic Characteristics of Cobalt Ferrite-Reduced Graphene Oxide and Cobalt Ferrite-Carbon Nanotube Nanocomposites. *J. Photochem. Photobiol., A* **2020**, *403*, No. 112867.
(49) Smith, A. T.; LaChance, A. M.; Zeng, S.; Liu, B.; Sun, L. Synthesis, Properties, and Applications of Graphene Oxide/Reduced Graphene Oxide and Their Nanocomposites. *Nano Mater. Sci.* **2019**, *1*, 31−47.
(50) Kotutha, I.; Duangchuen, T.; Swatsitang, E.; Meewasana, W.; Khajonrit, J.; Maensiri, S. Electrochemical Properties of RGO/CoFe2O4 Nanocomposites for Energy Storage Application. *Ionics* **2019**, *25*, 5401−5409.
(51) Schneider, C. A.; Rasband, W. S.; Eliceiri, K. W. NIH Image to ImageJ: 25 Years of Image Analysis. *Nat. Methods* **2012**, *9*, 671−675.
(52) Varma, P. C. R.; Manna, R. S.; Banerjee, D.; Varma, M. R.; Suresh, K. G.; Nigam, A. K. Magnetic Properties of CoFe2O4 Synthesized by Solid State, Citrate Precursor and Polymerized Complex Methods: A Comparative Study. *J. Alloys Compd.* **2008**, *453*, 298−303.
(53) Fahmi, A. H.; Samsuri, A. W.; Singh, D. Magnetization Improved Fine Particle Biochar Adsorption of Lead. *Soil Sediment Contam.* **2022**, *31*, 633−654.
(54) Wabaidur, S. M.; Khan, M. A.; Siddiqui, M. R.; Otero, M.; Jeon, B. H.; Alothman, Z. A.; Hakami, A. A. H. Oxygenated Functionalities Enriched MWCNTs Decorated with Silica Coated Spinel Ferrite − A Nanocomposite for Potentially Rapid and Efficient de-Colorization of Aquatic Environment. *J. Mol. Liq.* **2020**, *317*, No. 113916.
(55) Hu, L.; Li, M.; Cheng, L.; Jiang, B.; Ai, J. Solvothermal Synthesis of Octahedral and Magnetic CoFe2O4−Reduced Graphene Oxide Hybrids and Their Photo-Fenton-like Behavior under Visible-Light Irradiation. *RSC Adv.* **2021**, *11*, 22250−22263.
(56) Zhang, S.; Li, X. Y.; Chen, J. P. An XPS Study for Mechanisms of Arsenate Adsorption onto a Magnetite-Doped Activated Carbon Fiber. *J. Colloid Interface Sci.* **2010**, *343*, 232−238.
(57) Babaee, Y.; Mulligan, C. N.; Rahaman, M. S. Stabilization of Fe/Cu Nanoparticles by Starch and Efficiency of Arsenic Adsorption from Aqueous Solutions. *Environ. Earth Sci.* **2017**, *76*, 650.
(58) Singh, M.; Dosanjh, H. S.; Singh, H. Surface Modified Spinel Cobalt Ferrite Nanoparticles for Cationic Dye Removal: Kinetics and Thermodynamics Studies. *J. Water Process Eng.* **2016**, *11*, 152−161.
(59) Pochapski, D. J.; Carvalho Dos Santos, C.; Leite, G. W.; Pulcinelli, S. H.; Santilli, C. V. Zeta Potential and Colloidal Stability Predictions for Inorganic Nanoparticle Dispersions: Effects of Experimental Conditions and Electrokinetic Models on the Interpretation of Results. *Langmuir* **2021**, *37*, 13379−13389.
(60) Jacob, N. M.; Kuruva, P.; Madras, G.; Thomas, T. Purifying Water Containing Both Anionic and Cationic Species Using a (Zn, Cu)O, ZnO, and Cobalt Ferrite Based Multiphase Adsorbent System. *Ind. Eng. Chem. Res.* **2013**, *52*, 16384−16395.
(61) Singh, N.; Riyajuddin, S.; Ghosh, K.; Mehta, S. K.; Dan, A. Chitosan-Graphene Oxide Hydrogels with Embedded Magnetic Iron Oxide Nanoparticles for Dye Removal. *ACS Appl. Nano Mater.* **2019**, *2*, 7379−7392.
(62) Crini, G.; Badot, P. M. Application of Chitosan, a Natural Aminopolysaccharide, for Dye Removal from Aqueous Solutions by Adsorption Processes Using Batch Studies: A Review of Recent Literature. *Prog. Polym. Sci.* **2008**, *33*, 399−447.
(63) Benjelloun, M.; Miyah, Y.; Akdemir Evrendilek, G.; Zerrouq, F.; Lairini, S. Recent Advances in Adsorption Kinetic Models: Their Application to Dye Types. *Arab. J. Chem.* **2021**, *14*, No. 103031.
(64) Alarifi, I. M.; Al-Ghamdi, Y. O.; Darwesh, R.; Ansari, M. O.; Uddin, M. K. Properties and Application of MoS2 Nanopowder: Characterization, Congo Red Dye Adsorption, and Optimization. *J. Mater. Res. Technol.* **2021**, *13*, 1169−1180.
(65) Zhang, Y.; Yan, L.; Xu, W.; Guo, X.; Cui, L.; Gao, L.; Wei, Q.; Du, B. Adsorption of Pb(II) and Hg(II) from Aqueous Solution Using Magnetic CoFe2O4-Reduced Graphene Oxide. *J. Mol. Liq.* **2014**, *191*, 177−182.
(66) Huang, D.; Li, B.; Wu, M.; Kuga, S.; Huang, Y. Graphene Oxide-Based Fe-Mg (Hydr)Oxide Nanocomposite as Heavy Metals Adsorbent. *J. Chem. Eng. Data* **2018**, *63*, 2097−2105.
(67) Al Nafiey, A.; Addad, A.; Sieber, B.; Chastanet, G.; Barras, A.; Szunerits, S.; Boukherroub, R. Reduced Graphene Oxide Decorated with Co3O4 Nanoparticles (RGO-Co3O4) Nanocomposite: A Reusable Catalyst for Highly Efficient Reduction of 4-Nitrophenol, and Cr(VI) and Dye Removal from Aqueous Solutions. *Chem. Eng. J.* **2017**, *322*, 375−384.
(68) Song, Z. J.; Ran, W.; Wei, F. Y. One-Step Approach for the Synthesis of CoFe 2 o 4 @rGO Core-Shell Nanocomposites as Efficient Adsorbent for Removal of Organic Pollutants. *Water Sci. Technol.* **2017**, *75*, 397−405.
(69) Zhang, Q.; Cheng, Y.; Fang, C.; Chen, J.; Chen, H.; Li, H.; Yao, Y. Facile Synthesis of Porous Carbon/Fe3O4 Composites Derived from Waste Cellulose Acetate by One-Step Carbothermal Method as a Recyclable Adsorbent for Dyes. *J. Mater. Res. Technol.* **2020**, *9*, 3384−3393.
(70) Zhang, S.; Niu, H.; Cai, Y.; Zhao, X.; Shi, Y. Arsenite and Arsenate Adsorption on Coprecipitated Bimetal Oxide Magnetic Nanomaterials: MnFe2O4 and CoFe2O4. *Chem. Eng. J.* **2010**, *158*, 599−607.

https://doi.org/10.1021/acsomega.2c06636
ACS Omega 2023, 8, 6376−6390